Crustal fingering facilitates free-gas methane migration through the hydrate stability zone

Xiaojing Fu[a,b,1,2], Joaquin Jimenez-Martinez[c,d,e,1,2], Thanh Phong Nguyen[d], J. William Carey[d], Hari Viswanathan[d], Luis Cueto-Felgueroso[f], and Ruben Juanes[g,h,2]

[a]Department of Earth and Planetary Science, University of California, Berkeley, CA 94670; [b]Department of Mechanical and Civil Engineering, California Institute of Technology, Pasadena, CA 91125; [c]Department of Water Resources and Drinking Water, Swiss Federal Institute of Aquatic Science and Technology, Dubendorf 8600, Switzerland; [d]Earth and Environmental Sciences Division, Los Alamos National Laboratory, Los Alamos, NM 87545; [e]Department of Civil, Environmental and Geomatic Engineering, Swiss Federal Institute of Technology, Zurich 8093, Switzerland; [f]Department of Hydraulics, Energy and Environment, Technical University of Madrid, Madrid 28040, Spain; [g]Department of Civil and Environmental Engineering, Massachusetts Institute of Technology, Cambridge, MA 02139; and [h]Department of Earth, Atmospheric and Planetary Sciences, Massachusetts Institute of Technology, Cambridge, MA 02139

Edited by David A. Weitz, Harvard University, Cambridge, MA, and approved November 3, 2020 (received for review May 30, 2020)

Widespread seafloor methane venting has been reported in many regions of the world oceans in the past decade. Identifying and quantifying where and how much methane is being released into the ocean remains a major challenge and a critical gap in assessing the global carbon budget and predicting future climate [C. Ruppel, J. D. Kessler. Rev. Geophys. 55, 126–168 (2017)]. Methane hydrate ($CH_4 \cdot 5.75H_2O$) is an ice-like solid that forms from methane–water mixture under elevated-pressure and low-temperature conditions typical of the deep marine settings (>600-m depth), often referred to as the hydrate stability zone (HSZ). Wide-ranging field evidence indicates that methane seepage often coexists with hydrate-bearing sediments within the HSZ, suggesting that hydrate formation may play an important role during the gas-migration process. At a depth that is too shallow for hydrate formation, existing theories suggest that gas migration occurs via capillary invasion and/or initiation and propagation of fractures (Fig. 1). Within the HSZ, however, a theoretical mechanism that addresses the way in which hydrate formation participates in the gas-percolation process is missing. Here, we study, experimentally and computationally, the mechanics of gas percolation under hydrate-forming conditions. We uncover a phenomenon—*crustal fingering*—and demonstrate how it may control methane-gas migration in ocean sediments within the HSZ.

methane hydrate | pattern formation | microfluidics | phase-field method

A plethora of field observations, including Hydrate Ridge in the Cascadia margin (1–6), the Blake Ridge offshore northeast US continental margin (7), Hikurangi margin offshore New Zealand (8, 9), Vestnesa Ridge offshore west Svalbard (10–14), and a few other locations (15–19), suggests that free-gas methane venting can coexist with and persist within hydrate-bearing formations. Such coexistence is found in nature over a wide range of pressure, temperature, and compositional conditions. Yet, hydrate equilibrium thermodynamics predicts three-phase equilibrium only along the triple-point line (20, 21), which prescribes a precise set of pressure, temperature, and compositional conditions that are likely rare occurrences in marine settings. To explain the field observations, some argue that the coexistence of free gas, saline water, and hydrates is a true three-phase equilibrium facilitated by pore-scale effects, such as capillarity (22), salinity (23), or thermal anomalies (24). These effects modify the pressure (P) and temperature (T) at the triple point, allowing for more common occurrence of the three-phase coexistence. Others argue that the three-phase coexistence is, in fact, a thermodynamic nonequilibrium sustained by high rates of gas flux and slow kinetics of hydrate formation, as supported by field-scale observations (5, 25–27) and, more recently, by laboratory experiments at the core scale (28–30) and pore scale (31–33), as well as multiphase flow modeling (34–36). Despite much effort in understanding the problem from a thermodynamic perspective, few have addressed the fluid-mechanics puzzle of how the formation of solid hydrate, instead of clogging gas-migration pathways, can facilitate free gas flow in porous media.

Here, we address these questions by investigating the flow of hydrate-forming gas at the pore scale. We simplify the flow geometry within a porous medium or a self-propagating fracture to that of a Hele–Shaw cell, composed of two parallel plates separated by a thin gap (*SI Appendix*, Fig. S1*A*)—a classic and commonly used experimental analog for Darcy flow (37–40). Under hydrate-forming P, T conditions, we consider gas flow that is driven by an imposed fluid-pressure gradient generated by depressurization and gas compressibility, rather than buoyancy (*Materials and Methods*). The above simplifications allow us to focus on the two critical aspects of this problem: gas flow and hydrate formation.

In a quiescent multiphase environment consisting of a single gas bubble in a liquid water bath, we observed that the solidification of hydrate occurs along the gas–liquid interface to form a thin hydrate crust (Fig. 2*A* and Movie S1). This is analogous to the formation of hydrate crust on free-rising gas bubbles in the ocean (41) and offshore pipelines (42). Once the crust forms, the

Significance

Widespread seafloor methane venting has been reported in many regions of the world oceans, challenging our current estimate of global carbon budget. Yet, we still do not fully understand the fundamental mechanisms by which methane gas migrates through the deep marine sediments, feeding these vents. A key challenge is the formation of methane hydrate, an ice-like solid that forms from a methane–water mixture under pressure and temperature conditions typical of deep marine settings. Here, we study the mechanics of gas percolation under hydrate-forming conditions using experiments and computational modeling. We uncover a phenomenon, which we call crustal fingering, that helps explain how, counterintuitively, hydrate formation may facilitate instead of prevent methane gas migration through deep ocean sediments.

Author contributions: X.F., J.J.-M., T.P.N., J.W.C., L.C.-F., and R.J. designed research; X.F., J.J.-M., T.P.N., J.W.C., and H.V. performed research; X.F. and J.J.-M. analyzed data; and X.F., J.J.-M., J.W.C., L.C.-F., and R.J. wrote the paper.

The authors declare no competing interest.

This article is a PNAS Direct Submission.

[1]X.F. and J.J.-M. contributed equally to this work.

[2]To whom correspondence may be addressed. Email: rubyfu@caltech.edu, juanes@mit.edu, or joaquin.jimenez@eawag.ch.

This article contains supporting information online at https://www.pnas.org/lookup/suppl/doi:10.1073/pnas.2011064117/-/DCSupplemental.

First published November 30, 2020.

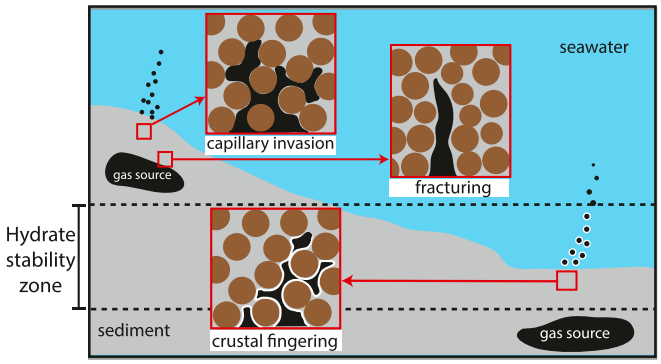

Fig. 1. Methane-gas migration through shallow marine environment and the hydrate stability zone. Shown is a representation of a methane-rich gas reservoir (black) feeding the upward migration of methane gas through the seafloor sediments (gray) into the ocean-water column (blue), forming seafloor methane seeps (bubbly plume). The methane HSZ on earth is approximately 600 to 1,400 m below the ocean surface. (*Upper Insets*) Two primary modes of gas migration in shallow sediments are 1) *capillary invasion* in a rigid-like sediment, where gas pressure overcomes capillary force to move between sediment pores, and 2) *fracturing*, where gas pressure is sufficient to mobilize sediment grains to initiate and propagate fractures. (*Lower Inset*) A mode of methane-gas migration within the HSZ proposed in this work: *crustal fingering*.

extremely slow diffusion of water and methane within hydrate hinders its continued growth (43–45). As a result, the interfacial hydrate grows to a finite thickness within the time scale of the experiment (Fig. 2*A*) and serves as a *transport barrier* for further exchange across the interface (34, 46).

As we induce gas flow through depressurization at a constant rate (*SI Appendix*), the interfacial hydrate crust serves not only as a transport barrier, but also as a *flow resistor*. Inspection of the experiment (Fig. 2*C* and Movie S2) suggests that three primary mechanisms control the observed gas-migration pattern (Fig. 2*B*): crust rupturing, gas flow, and crust formation. Because the hydrate crust is rigid, it takes a threshold pressure across the hydrate layer before it ruptures at a point and releases the entrapped gas. Crust rupturing occurs repeatedly and intermittently during the experiments (Fig. 2*C*, magenta circles; see also refs. 29 and 30) and is likely controlled by the local pressure difference and crust tensile strength (47–50). The location of the thinnest crust corresponds to weaker tensile strength and, thus, is more prone to rupture. Due to the subcooling effect on hydrate growth rate (33), crust that forms later in the experiment grows more slowly and, thus, appears thinner (*SI Appendix*, Fig. S3). Once the gas breaks through, its continued flow creates additional gas–liquid interface, promoting the formation of hydrate at the interface. The gas finger continues its movement until a combination of reduced driving pressure and thickened crust fully arrests its flow, at which point the crust ruptures at a different location to give birth to a new fingering branch. Under these coupled processes, the displacement of gas into liquid does not follow that of typical two-phase flow through fractures and porous media [e.g., viscous fingering or stable displacement (38)]. A new pattern of gas percolation emerges, where continuous gas flow modulated by the spontaneous interfacial hydrate formation leads to the evolution of crustal gas fingers, or *crustal fingering* (Fig. 2*C*).

We describe the key observations of the experiments using a phase-field model (*Materials and Methods* and *SI Appendix*), which incorporates the primary mechanisms of gas flow and crust formation and captures the crustal fingering pattern qualitatively (Fig. 3*A* and Movie S3). The rate of depressurization or gas flow, Q_{outlet}, enters through the mass conservation equation as a boundary condition. The rate of hydrate formation R_s, which is determined by local thermodynamic forcing such as subcooling, is imposed in our model. A larger R_s corresponds to a stronger subcooling and a faster rate of hydrate crust formation (33) (*SI Appendix*, Fig. S3). Our model does not describe the mechanics of crust rupturing, and we do not include thermal or salinity effects in the thermodynamic component of the model.

Additional simulations with our model suggest that, once the crust ruptures, the competition between local gas-flow rate (imposed by Q_{outlet}) and crust-formation rate (controlled by R_s) is crucial in determining the pattern and dynamics of gas migration (Fig. 3*B*). When hydrate forms significantly faster than gas flows, the crust can fully arrest gas flow (Fig. 3*B*, red outline)—a scenario likely responsible for the clogging behavior observed in gas conduits in the field (51, 52) and intermittent flow dynamics observed in core-scale experiments (29, 30). When hydrate does not form, our model recovers stable gas expansion expected for regular gas bubbles (Fig. 3*B*, blue outline). The rest of the phase diagram suggests a wide range of conditions that allow for continuous gas displacement in the form of a single meandering crustal finger (Fig. 3, yellow outline) or multiple fingering branches (Fig. 3*B*, green outline). These crustal fingers serve as preferential pathways that facilitate gas flow. Additional experiments under different depressurization rates (Fig. 3*C*) and simulations (Fig. 3*B*, $R_s = 1/0.8$) both suggest that crustal finger width is regulated by the imposed flow rate: A higher flow rate leads to wider finger channels.

The rich dynamics of crustal fingering provides clues to understand gas migration within the hydrate stability zone (HSZ): When the local gas-flow rate is sufficiently high, hydrate formation does not necessarily clog fluid pathways, but, instead, can

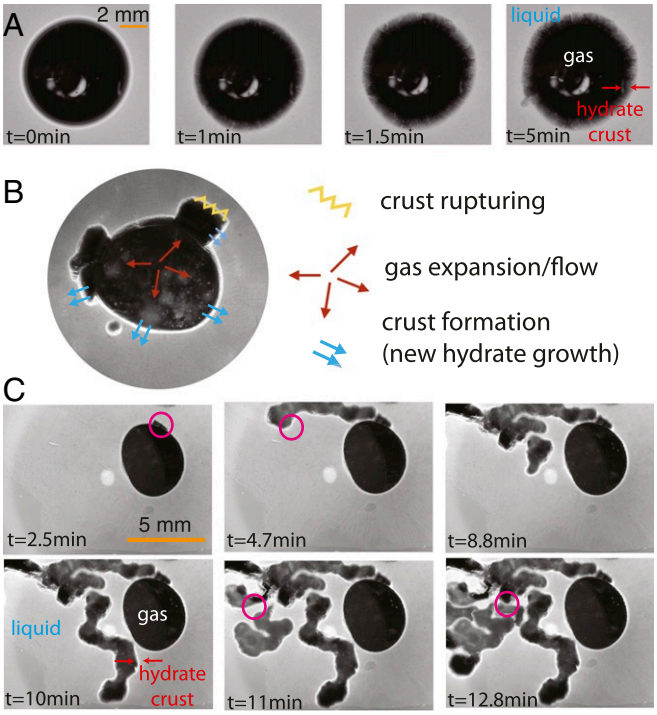

Fig. 2. Experimental observations of hydrate crust formation and crustal fingering. (*A*) During a quiescent experiment, an initially smooth Xe bubble surface becomes rougher as hydrate crust forms on the gas–liquid interface. (*B*) Three primary mechanisms that control crustal fingering dynamics. (*C*) Snapshots during a depressurization experiment at 0.5 MPa/min (that induces expansion and gas flow). The magenta circles mark locations of crust rupturing, which do not always coincide with the front of the gas finger because the entire length of the crust is susceptible to break.

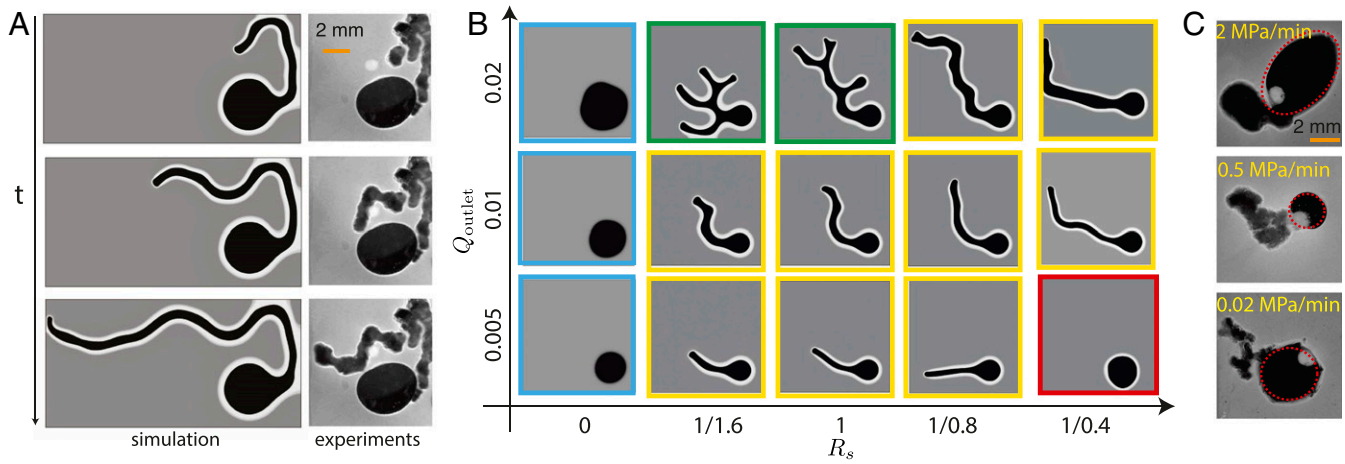

Fig. 3. Meandering dynamics and pattern formation of crustal fingering. (*A*) Simulation snapshots showing gas (black) fingers into the ambient liquid (dark gray) while encrusted by a layer of hydrate (white). (*A*, *Right*) Experimental snapshots showing similar meandering behavior of a hydrate-crusted gas finger (depressurizing at 0.5 MPa/min). Note the experimental images are from the same experiment shown in Fig. 2 and have been rotated 90° clockwise. (*B*) Phase diagram of gas-migration behavior illustrated by simulated patterns at $t = 24$ for a gas bubble expanding in a square domain under various Q_{outlet} and R_s. $R_s = 0$ corresponds to simulations where hydrate does not form. (*C*) Snapshots from three experiments with different depressurization rates. The dashed red circles mark the original gas bubbles, outside of which crustal fingers are formed during depressurization. The finger width decreases with decreasing depressurization rate.

form hydrate-encrusted channel that facilitates gas flow. Such insight informs our understanding of the temporal variability and spatial organization of subsurface gas migration at the field scale. To illustrate this, we simulated field-scale gas migration fueled by periodic recharge events below the Bottom Simulating Reflector (*SI Appendix*, Fig. S4). We considered that gas is supplied by a deep source (53) with periodic recharge episodes and parameterize its dynamics by its recharge frequency (f) and episode strength (Q_{in}) (Fig. 4*A*). We assumed a uniform sediment permeability and did not consider preexisting faults or fractures that could dominate flow pathways. To our surprise, we found that coupling time-varying gas flow with concurrent hydrate solidification is sufficient to recover several hydrate-derived features commonly observed in the field (Fig. 4 *B* and *C* and Movie S4). When recharge episodes are strong (Fig. 4 *B* and *C*, *Upper*), our model predicts the formation of vertical and hydrate-walled gas conduits (10, 52, 54, 55) that sometimes terminate before reaching the seafloor (8, 9). The spatial density of conduits appears to decrease with decreasing recharge frequency. When recharge episodes are weak and infrequent (Fig. 4 *B* and *C*, *Left Lower*), upward gas flow becomes completely arrested to form hydrate-crusted gas pockets (56). However, when recharge episodes are weak, but frequent (Fig. 4 *B* and *C*, *Right Lower*), the interactions among conduits become highly nonlinear and form complex patterns. The subsurface hydrate fabric becomes multitextured, consisting of vertical conduits, lateral conduits, gas pockets, and clogged conduits, as has been observed in the field (8, 9). During these complex interactions, it is the availability of local gas pressure that determines whether a conduit will sustain its upward growth, divert laterally, or terminate.

In the current study, we do not consider the mechanical interactions among the fluids, solid hydrates, and sediment grains and how they may affect gas migration. In particular, as fluid-driven fracturing is a prevalent mode of gas transport in soft sediments (56–59) and often concurs with hydrate growth (9, 28, 54), one would need to model both the fracturing (60–63) and the crustal fingering process to fully resolve the fluid–grain mechanics at the pore scale. Therefore, our model does not directly address the open question of what determines the dominant modes of hydrate occurrence within sediments at the core scale (64). Nevertheless, our mechanistic description of crustal fingering provides a crucial fluid-mechanics piece to decipher the puzzle of how methane gas migrates through the hydrate stability zone (Fig. 1) and offers an alternative to existing theories of gas migration (36). In addition, while it is commonly accepted that most marine hydrates on Earth have formed out of dissolved methane that has previously migrated in place or

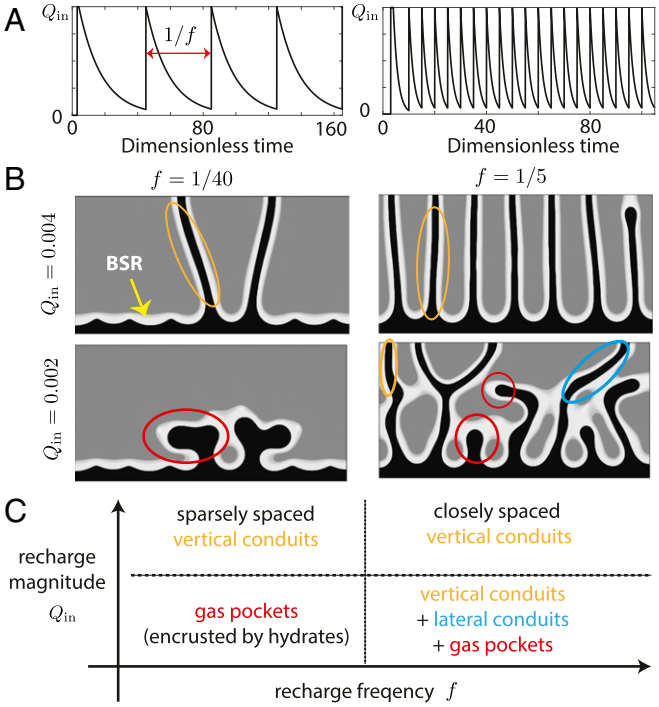

Fig. 4. Subsurface hydrate fabric as shaped by crustal fingering processes. (*A*) Time series of imposed gas flux at the bottom boundary, representing infrequent (*Left*) and frequent (*Right*) recharging. (*B*) Simulation snapshot at $t = 105$ for different recharge frequencies (*Left* and *Right*) and for strong (*Upper*) and weak (*Lower*) recharge episodes. BSR, Bottom Simulating Reflector. (*C*) Different types of hydrate-derived features evolve, depending on different styles of recharge dynamics.

generated in situ biogenically (36, 65), our work suggests that, at the geologic field scale, some of the subsurface hydrate fabric we observe today could be a record of the dynamic history of deep-sea methane venting coupled with the formation of hydrate along the gas-migration pathways within the marine sediments over long periods of time (5). The theoretical framework we propose (Fig. 4), although lacking details of geologic features (e.g., faults or preferential pathways), can be a good starting point to connect the increasing amount of seafloor data on methane-venting dynamics (6, 17, 66) with geophysical constraints on the subsurface hydrate-derived plumbing structure (8–10, 26, 55, 67) to answer the question of where and how much methane is being released into the ocean through these naturally occurring methane seeps (68).

Materials and Methods

Laboratory Experiments. We conducted experiments using a high-pressure microfluidic device developed at Los Alamos National Laboratory (69). The microfluidic Hele–Shaw cell (*SI Appendix*, Fig. S1*A*) was made of two parallel glass plates with dimensions 14 mm ×14 mm and a gap thickness of 1 mm. The entire cell was sealed off and pressurized within a high-pressure flow loop maintained at a constant temperature of 25 °C. We imaged the experiments using a charge-coupled device camera (Olympus DP72), which recorded the experiments through a microscope (Olympus MVX10) positioned in front of the viewing window of the high-pressure device. We adopted xenon (Xe) and water (H_2O) as the experimental analogue to the methane hydrates system. This choice was made for the following reasons: 1) Xe hydrates form at more easily accessible experimental conditions; 2) both Xe and methane form structure I hydrate up to 1.8 GPa, which is the most common structure observed in nature; and 3) Xe–water and methane–water system exhibit similar thermodynamic phase behaviors (46). We are not aware of studies that report the mechanical properties (e.g., tensile strength) of Xe hydrate. However, based on similar studies of CO_2 hydrate (48), we speculate that Xe hydrates and CH_4 hydrates are mechanically similar. Any difference in their mechanical properties will not fundamentally change the primary mechanisms that make up crustal fingering—crust rupture, gas flow, and new crust growth.

There were two ports that controlled fluid input to and output from the cell. To prepare the experiments, we first injected deionized water through the water port to fill the entire gap at ambient pressure. Then, a bubble of Xe gas was introduced into the water bath through the Xe port. Next, in order to pressurize the system to hydrate-forming conditions (P = 7.5 MPa and T = 25 °C), we closed off the water port while keeping the Xe gas bubble connected to a pressure-valve-controlled Xe gas supply. This ensured that the gas phase could be readily replenished and stay pressurized instead of dissolving into water at a higher pressure. We kept the system pressurize at P = 7.5 MPa and obtained visual confirmation that a hydrate shell had formed along the gas–liquid interface (Movie S1). Once the hydrate-crusted gas bubble was established, we induced gas flow in the domain by depressurizing the entire cell via fluid withdrawal from the water port. Prior to depressurization, we closed off the Xe port to ensure that no additional gas would be introduced into the system. We imposed a constant rate of depressurization (0.02, 0.5, and 2 MPa/min) at the water port.

In *SI Appendix*, we provide additional details on the validation of solid hydrate formation in the experiments, as well as a discussion on the effects of subcooling on the crustal fingering process.

Phase-Field Modeling. We develop a continuum-scale phase-field model to study gas–liquid–hydrate systems far from thermodynamic equilibrium (34). In this model, we tracked the volumetric fractions of fluid/solid phases (ϕ_α), as well as the pointwise mole fraction of Xe (χ). We started by designing a simplified Gibbs free energy (F) for the three phases (gas, liquid, and hydrate) as a function of χ and temperature (T) (*SI Appendix*). The proposed free energy F was incorporated into a phase-field model to study the nonequilibrium thermodynamics of the three-phase system. The evolution of the system variables (χ and ϕ_α) was driven by potentials Ψ, which are variational derivatives of F. To describe the evolution dynamics, we start by imposing mass conservation of the total mixture (Xe plus water):

$$\frac{\partial \rho}{\partial t} + \nabla \cdot (\rho \mathbf{u}) = 0. \quad [1]$$

Additionally, we prescribe the conservation of mass of Xe using a Cahn–Hilliard-type equation for χ:

$$\frac{\partial \rho \chi}{\partial t} + \nabla \cdot (\rho \chi \mathbf{u}) - R_\chi \nabla \cdot (D(\{\phi_\alpha\})\rho \nabla \Psi_c) = 0. \quad [2]$$

We complete the system with a nonconserved Allen–Cahn evolution equation for ϕ_α in an advective form:

$$\frac{\partial \phi_\alpha}{\partial t} + \mathbf{u} \cdot \nabla \phi_\alpha + R_\phi \Psi_\alpha = 0. \quad [3]$$

The evolution equations are then coupled with a simplified description for three-phase Hele–Shaw flow (70):

$$\mathbf{u}(x, y) = \frac{-k}{\mu(\phi_g, \phi_l, \phi_s)} \nabla p. \quad [4]$$

The full details of the model are provided in *SI Appendix*.

Numerical Simulations. We discretized all of the equations using finite elements and adopted a two-step segregated solution strategy to solve the system of equations. In step one, the system of four constrained partial differential equations in Eqs. **2** and **3** were solved by using a monolithically coupled implicit time integration scheme. In step 2, the pressure problem, as prescribed by Eq. **4** and Eq. **1**, was solved implicitly by using updated phase solutions from step 1. Time steps were determined dynamically to ensure stability and convergence. Additional details on the laboratory-scale and field-scale simulations are provided in *SI Appendix*.

Data Availability. All study data are included in the article and *SI Appendix*.

ACKNOWLEDGMENTS. We thank Carolyn Ruppel and William Waite from the US Geological Survey; Peter Flemings, Kehua You, and Dylan Meyer from the University of Texas at Austin; Gareth Crutchley from GEOMAR Helmholtz Centre for Ocean Research Kiel for insightful discussions; and David Santillán (Technical University of Madrid) and Ehsan Haghigat (MIT) for help with the code development. This work was supported in part by the US Department of Energy Grants DE-SC0018357 and DE-FE0013999. X.F. was supported by the Miller Fellowship. J.J.-M. was supported by Swiss Federal Institute of Aquatic Science and Technology and Guest Scientist status from Los Alamos National Laboratory. J.J.-M., J.W.C., T.P.N., and H.V. were supported by US Department of Energy Basic Energy Science Program Grant LANLE3W1. L.C.-F. was supported by Spanish Ministry of Economy and Competitiveness Grants RYC-2012-11704 and CTM2014-54312-P. L.C.-F. and R.J. were supported by MIT International Science and Technology Initiatives, through a Seed Fund grant.

1. E. Suess *et al.*, Gas hydrate destabilization: Enhanced dewatering, benthic material turnover and large methane plumes at the Cascadia convergent margin. *Earth Planet Sci. Lett.* **170**, 1–15 (1999).
2. P. Linke *et al.*, In situ measurement of fluid flow from cold seeps at active continental margins. *Deep Sea Res. Pt. I* **41**, 721–739 (1994).
3. W. T. Wood, J. F. Gettrust, N. R. Chapman, G. D. Spence, R. D. Hyndman, Decreased stability of methane hydrates in marine sediments owing to phase-boundary roughness. *Nature* **420**, 656–660 (2002).
4. K. U. Heeschen, A. M. Tréhu, R. W. Collier, E. Suess, G. Rehder, Distribution and height of methane bubble plumes on the Cascadia Margin characterized by acoustic imaging. *Geophys. Res. Lett.* **30**, 1643 (2003).
5. M. Haeckel, E. Suess, K. Wallmann, D. Rickert, Rising methane gas bubbles form massive hydrate layers at the seafloor. *Geochem. Cosmochim. Acta* **68**, 4335–4345 (2004).
6. M. Riedel *et al.*, Distributed natural gas venting offshore along the Cascadia margin. *Nat. Commun.* **9**, 3264 (2018).
7. A. R. Gorman *et al.*, Migration of methane gas through the hydrate stability zone in a low-flux hydrate province. *Geology* **30**, 327–330 (2002).
8. S. Koch *et al.*, Gas-controlled seafloor doming. *Geology* **43**, 571–574 (2015).
9. M. Riedel *et al.*, Elongate fluid flow structures: Stress control on gas migration at Opouawe Bank, New Zealand. *Mar. Petrol. Geol.* **92**, 913–931 (2018).
10. C. J. Petersen, S. Bünz, S. Hustoft, J. Mienert, D. Klaeschen, High-resolution P-Cable 3D seismic imaging of gas chimney structures in gas hydrated sediments of an Arctic sediment drift. *Mar. Petrol. Geol.* **27**, 1981–1994 (2010).
11. S. Bünz, S. Polyanov, S. Vadakkepuliyambatta, C. Consolaro, J. Mienert, Active gas venting through hydrate-bearing sediments on the Vestnesa Ridge. Offshore W-Svalbard. *Mar. Geol.* **332–334**, 189–197 (2012).

12. A. J. Smith, J. Mienert, S. Bunz, J. Greinert, Thermogenic methane injection via bubble transport into the upper Arctic Ocean from the hydrate-charged Vestnesa Ridge. Svalbard. *Geochem. Geophys. Geosyst.* **15**, 1945–1959 (2014).
13. A. Plaza-Faverola *et al.*, Role of tectonic stress in seepage evolution along the gas hydrate-charged Vestnesa Ridge, Fram Strait. *Geophys. Res. Lett.* **42**, 733–742 (2015).
14. A. Plaza-Faverola *et al.*, Bottom-simulating reflector dynamics at Arctic thermogenic gas provinces: An example from Vestnesa Ridge, offshore west Svalbard. *J. Geophys. Res. Solid Earth* **122**, 4089–4105 (2017).
15. N. Shakhova *et al.*, Extensive methane venting to the atmosphere from sediments of the East Siberian Arctic Shelf. *Science* **327**, 1246–50 (2010).
16. N. Shakhova *et al.*, Ebullition and storm-induced methane release from the East Siberian Arctic Shelf. *Nat. Geosci.* **7**, 64–70 (2014).
17. A. Skarke, C. Ruppel, M. Kodis, D. Brothers, E. Lobecker, Widespread methane leakage from the sea floor on the northern US Atlantic margin. *Nat. Geosci.* **7**, 657–661 (2014).
18. C. Berndt *et al.*, Temporal constraints on hydrate-controlled methane seepage off Svalbard. *Science* **343**, 284–288 (2014).
19. J. Knies *et al.*, Modelling persistent methane seepage offshore western Svalbard since early Pleistocene. *Mar. Petrol. Geol.* **91**, 800–811 (2018).
20. E. D. Sloan, C. A. Koh, *Clathrate Hydrates of Natural Gases* (CRC Press, Boca Raton, FL, ed. 3, 2008).
21. E. D. Sloan, C. A. Koh, A. K. Sum, Gas hydrate stability and sampling: The future as related to the phase diagram. *Energies* **3**, 1991–2000 (2010).
22. M. B. Clennell, M. Hovland, J. S. Booth, P. Henry, W. J. Winters, formation of natural gas hydrates in marine sediments: 1. Conceptual model of gas hydrate growth conditioned by host sediment properties. *J. Geophys. Res. Solid Earth* **104**, 22985–23003 (1999).
23. X. Liu, P. B. Flemings, Passing gas through the hydrate stability zone at southern Hydrate Ridge, offshore Oregon. *Earth Planet Sci. Lett.* **241**, 211–226 (2006).
24. I. A. Pecher *et al.*, A fluid pulse on the Hikurangi subduction margin: Evidence from a heat flux transect across the upper limit of gas hydrate stability. *Geophys. Res. Lett.* **44**, 12,385–12,395 (2017).
25. W. Xu, C. Ruppel, Predicting the occurrence, distribution, and evolution of methane gas hydrate in porous marine sediments. *J. Geophys. Res. Solid Earth* **104**, 5081–5095 (1999).
26. A. M. Tréhu *et al.*, Feeding methane vents and gas hydrate deposits at south Hydrate Ridge. *Geophys. Res. Lett.* **31**, L23310 (2004).
27. M. Torres *et al.*, Gas hydrate growth, methane transport, and chloride enrichment at the southern summit of Hydrate Ridge, Cascadia margin off Oregon. *Earth Planet Sci. Lett.* **226**, L23310 (2004).
28. L. Lei, J. C. Santamarina, Laboratory strategies for hydrate formation in fine-grained sediments. *J. Geophys. Res. Solid Earth* **123**, 2583–2596 (2018).
29. D. W. Meyer *et al.*, Experimental investigation of gas flow and hydrate formation within the hydrate stability zone. *J. Geophys. Res. Solid Earth* **123**, 5350–5371 (2018).
30. D. W. Meyer, P. B. Flemings, D. DiCarlo, Effect of gas flow rate on hydrate formation within the hydrate stability zone. *J. Geophys. Res. Solid Earth* **123**, 6263–6276 (2018).
31. M. Chaouachi *et al.*, Microstructural evolution of gas hydrates in sedimentary matrices observed with synchrotron X-ray computed tomographic microscopy. *Geochem. Geophys. Geosyst.* **16**, 1711–1722 (2015).
32. S. K. Sahoo *et al.*, Laboratory insights into the effect of sediment-hosted methane hydrate morphology on elastic wave velocity from time-lapse 4D synchrotron X-ray computed tomography. *Geochem. Geophys. Geosyst.* **19**, 4502–4521 (2018).
33. A. Touil, D. Broseta, A. Desmedt, Gas hydrate crystallization in thin glass capillaries: Roles of supercooling and wettability. *Langmuir* **35**, 12569–12581 (2019).
34. X. Fu, L. Cueto-Felgueroso, R. Juanes, Nonequilibrium thermodynamics of hydrate growth on a gas a liquid interface. *Phys. Rev. Lett.* **120**, 144501 (2018).
35. D. W. Meyer, P. B. Flemings, K. You, D. A. DiCarlo, Gas flow by invasion percolation through the hydrate stability zone. *Geophys. Res. Lett.* **47**, e2019GL084380 (2020).
36. K. You, P. B. Flemings, A. Malinverno, T. S. Collett, K. Darnell, Mechanisms of methane hydrate formation in geological systems. *Rev. Geophys.* **57**, 1146–1196 (2019).
37. H. Hele-Shaw, The flow of water. *Nature* **58**, 34–36 (1898).
38. G. M. Homsy, Viscous fingering in porous media. *Annu. Rev. Fluid Mech.* **19**, 271–311 (1987).
39. B. Sandnes, E. G. Flekkøy, H. A. Knudsen, K. J. Måløy, H. See, Patterns and flow in frictional fluid dynamics. *Nat. Commun.* **2**, 288 (2011).
40. T. T. Al-Housseiny, P. A. Tsai, H. A. Stone, Control of interfacial instabilities using flow geometry. *Nat. Phys.* **8**, 747–750 (2012).
41. R. P. Warzinski *et al.*, Dynamic morphology of gas hydrate on a methane bubble in water: Observations and new insights for hydrate film models. *Geophys. Res. Lett.* **41**, 6841–6847 (2014).
42. Z. M. Aman, C. A. Koh, Interfacial phenomena in gas hydrate systems. *Chem. Soc. Rev.* **45**, 1678–1690 (2016).
43. Y. Abe, X. Ma, T. Yanai, K. Yamane, Development of formation and growth models of CO_2 hydrate film. *AIChE J.* **62**, 4078–4089 (2016).
44. B. Kvamme, A. Svandal, T. Buanes, T. Kuznetsova, "Phase field approaches to the kinetic modeling of hydrate phase transitions" in *Natural Gas Hydrates—Energy Resource Potential and Associated Geologic Hazards*, T. Collett, A. Johnson, C. Knapp, R. Boswell, Eds. (AAPG Memoir, American Association of Petroleum Geologists, Tulsa, OK, 2009), vol. 89, pp. 758–769.
45. C. J. Taylor, K. T. Miller, C. A. Koh, E. D. Sloan, Macroscopic investigation of hydrate film growth at the hydrocarbon/water interface. *Chem. Eng. Sci.* **62**, 6524–6533 (2007).
46. X. Fu, W. F. Waite, L. Cueto-Felgueroso, R. Juanes, Xenon hydrate as an analogue of methane hydrate in geologic systems out of thermodynamic equilibrium. *Geochem. Geophys. Geosyst.* **20**, 2462–2472 (2019).
47. S. R. Davies, E. D. Sloan, A. K. Sum, C. A. Koh, In situ studies of the mass transfer mechanism across a methane hydrate film using high-resolution confocal Raman spectroscopy. *J. Phys. Chem. C* **114**, 1173–1180 (2010).
48. J. W. Jung, J. C. Santamarina, Hydrate adhesive and tensile strengths. *Geochem. Geophys. Geosyst.* **12**, 1–9 (2011).
49. J. Wu *et al.*, Mechanical instability of monocrystalline and polycrystalline methane hydrates. *Nat. Commun.* **6**, 8743 (2015).
50. D. Atig, D. Broseta, J. M. Pereira, R. Brown, Contactless probing of polycrystalline methane hydrate at pore scale suggests weaker tensile properties than thought. *Nat. Commun.* **11**, 3379 (2020).
51. A. V. Egorov, P. P. Shirshov, K. Crane, P. R. Vogt, A. N. Rozhkov, Gas hydrates that outcrop on the sea floor: Stability models. *Geo Mar. Lett.* **19**, 68–75 (1999).
52. N. L. B. Bangs, M. J. Hornbach, C. Berndt, The mechanics of intermittent methane venting at South Hydrate Ridge inferred from 4D seismic surveying. *Earth Planet Sci. Lett.* **310**, 105–112 (2011).
53. J. Nimblett, C. Ruppel, Permeability evolution during the formation of gas hydrates in marine sediments. *J. Geophys. Res. Solid Earth* **108**, 2420 (2003).
54. M. Riedel *et al.*, Geophysical and geochemical signatures associated with gas hydrate related venting in the northern Cascadia margin. *Geol. Soc. Am. Bull.* **118**, 23–38 (2006).
55. A. Plaza-Faverola, S. Bünz, J. Mienert, The free gas zone beneath gas hydrate bearing sediments and its link to fluid flow: 3-D seismic imaging offshore mid-Norway. *Mar. Geol.* **291-294**, 211–226 (2012).
56. M. J. Hornbach, D. M. Saffer, W. S. Holbrook, Critically pressured free-gas reservoirs below gas-hydrate provinces. *Nature* **427**, 142–144 (2004).
57. P. B. Flemings, X. Liu, W. J. Winters, Critical pressure and multiphase flow in Blake Ridge gas hydrates. *Geology* **31**, 1057 (2003).
58. B. P. Boudreau *et al.*, Bubble growth and rise in soft sediments. *Geology* **33**, 517 (2005).
59. B. P. Scandella, K. Delwiche, H. F. Hemond, R. Juanes, Persistence of bubble outlets in soft, methane-generating sediments. *J. Geophys. Res. Biogeosci.* **122**, 1298–1320 (2017).
60. A. K. Jain, R. Juanes, Preferential mode of gas invasion in sediments: Grain-scale mechanistic model of coupled multiphase fluid flow and sediment mechanics. *J. Geophys. Res. Solid Earth* **114**, B08101 (2009).
61. R. Holtzman, M. L. Szulczewski, R. Juanes, Capillary fracturing in granular media. *Phys. Rev. Lett.* **108**, 264504 (2012).
62. Z. Sun, J. C. Santamarina, Grain-displacive gas migration in fine-grained sediments. *J. Geophys. Res. Solid Earth* **124**, 2274–2285 (2019).
63. Y. Meng, B. K. Primkulov, Z. Yang, C. Y. Kwok, R. Juanes, Jamming transition and emergence of fracturing in wet granular media. *Phys. Rev. Res.* **2**, 022012 (2020).
64. W. F. Waite *et al.*, Physical properties of hydrate-bearing sediments. *Rev. Geophys.* **47**, RG4003 (2009).
65. C. D. Ruppel, W. F. Waite, Timescales and processes of methane hydrate formation and breakdown, with application to geologic systems. *J. Geophys. Res. Solid Earth* **125**, e2018JB016459 (2020).
66. B. Wang, S. Socolofsky, J. Breier, J. Seewald, Observations of bubbles in natural seep flares at MC 118 and GC 600 using in situ quantitative imaging. *J. Geophys. Res. Oceans* **121**, 2203–2230 (2016).
67. K. Andreassen *et al.*, Massive blow-out craters formed by hydrate-controlled methane expulsion from the Arctic seafloor. *Science* **356**, 948–953 (2017).
68. C. Ruppel, J. D. Kessler, The interaction of climate change and methane hydrates. *Rev. Geophys.* **55**, 126–168 (2017).
69. M. L. Porter *et al.*, Geo-material microfluidics at reservoir conditions for subsurface energy resource applications. *Lab Chip* **15**, 4044–4053 (2015).
70. L. Cueto-Felgueroso, R. Juanes, A phase-field model of two-phase Hele-Shaw flow. *J. Fluid Mech.* **758**, 522–552 (2014).